Supporting Online Material for

# Observation of Unconventional Quantum Spin Textures in Topologically Ordered Materials

D. Hsieh, Y. Xia, L. Wray, D. Qian, A. Pal, J. H. Dil, F. Meier, J. Osterwalder, G. Bihlmayer, C. L. Kane, Y. S. Hor, R. J. Cava, M. Z. Hasan*

*To whom correspondence should be addressed. E-mail: mzhasan@princeton.edu

Published 13 February 2009, *Science* **323**, 919 (2008)
DOI: 10.1126/science.1167733

**This PDF file includes:**

# Supporting Online Material: Observation of unconventional quantum spin textures in topologically ordered materials

D. Hsieh[1], Y. Xia[1,2], L. Wray[1,3], D. Qian[1], A. Pal[1], J.H. Dil[4,5], F. Meier[4,5], J. Osterwalder[5], G. Bihlmayer[6], C.L. Kane[7], Y.S. Hor[8], R.J. Cava[8] and M.Z. Hasan[1,2]



## SOM A. Materials and Methods

Spin-integrated angle-resolved photoemission spectroscopy (ARPES) measurements were performed with 14 to 30 eV photons on beam line 5-4 at the Stanford Synchrotron Radiation Laboratory, and with 28 to 32 eV photons on beam line 12 at the Advanced Light Source, both endstations being equipped with a Scienta hemispherical electron analyzer (see VG Scienta manufacturer website for instrument specifications). Spin-resolved ARPES measurements were performed at the SIS beam line at the Swiss Light Source using the COPHEE spectrometer (S1, p.15) with a single 40 kV classical Mott detector and photon energies of 20 and 22 eV. The typical energy and momentum resolution was 15 meV and 1.5% of the surface Brillouin zone (BZ) respectively at beam line 5-4, 9 meV and 1% of the surface BZ respectively at beam line 12, and 80 meV and 3% of the surface BZ respectively

at SIS using a pass energy of 3 eV. The undoped and Te doped $Bi_{1-x}Sb_x$ single crystal samples were each cleaved from a boule grown from a stoichiometric mixture of high purity elements. The boule was cooled from 650 to 270 °C over a period of 5 days and was annealed for 7 days at 270 °C. Our ARPES results were reproducible over many different sample batches. Determination of the Sb compositions in $Bi_{1-x}Sb_x$ to 1% precision was achieved by bulk resistivity measurements, which are very sensitive to Sb concentration (23), as well as scanning electron microscopy analysis on a cleaved surface showing lateral compositional homogeneity over the length scale of our ARPES photon beam size. X-ray diffraction (XRD) measurements were used to check that the samples were single phase, and confirmed that the single crystals presented in this paper have rhombohedral A7 crystal structure (point group $R\bar{3}m$). The XRD patterns of the cleaved crystals exhibit only the (333), (666), and (999) peaks showing that the naturally cleaved surface is oriented along the trigonal (111) axis. Room temperature data were recorded on a Bruker D8 diffractometer using Cu K$\alpha$ radiation ($\lambda$=1.54 Å) and a diffracted beam monochromator. The in-plane crystal orientation was determined by Laue x-ray diffraction prior to insertion into an ultra high vacuum environment. Cleaving these samples *in situ* between 10 K and 55 K at chamber pressures less than 5 $\times 10^{-11}$ torr resulted in shiny flat surfaces, characterized *in situ* by low energy electron diffraction (LEED) to be clean and well ordered with the same symmetry as the bulk [Fig. S2(B)]. This is consistent with photoelectron diffraction measurements that show no substantial structural relaxation of the Sb(111) surface (S2).

## SOM B. Two-step fitting analysis procedure of Spin-Resolved ARPES measurements of insulating $Bi_{1-x}Sb_x$

Here we present details of the spin-resolved ARPES analysis on bulk insulating $Bi_{0.91}Sb_{0.09}$ that show how we arrive at a spin-resolved surface band dispersion such as that presented in Figure 1(G) in the main text. In the VUV incident photon energy regime that we use, spin conserving photoemission processes (where the electric field of light only acts on the orbital degree of freedom of the electron inside a solid) dominate over spin non-conserving processes (which arise from coupling to the magnetic field of light) (S3). Therefore we are confident that the photo-emission process does not change the spin polarization of the electrons. Figure S1(B) shows a spin averaged momentum distribution curve (MDC) along the $\bar{\Gamma}$ to

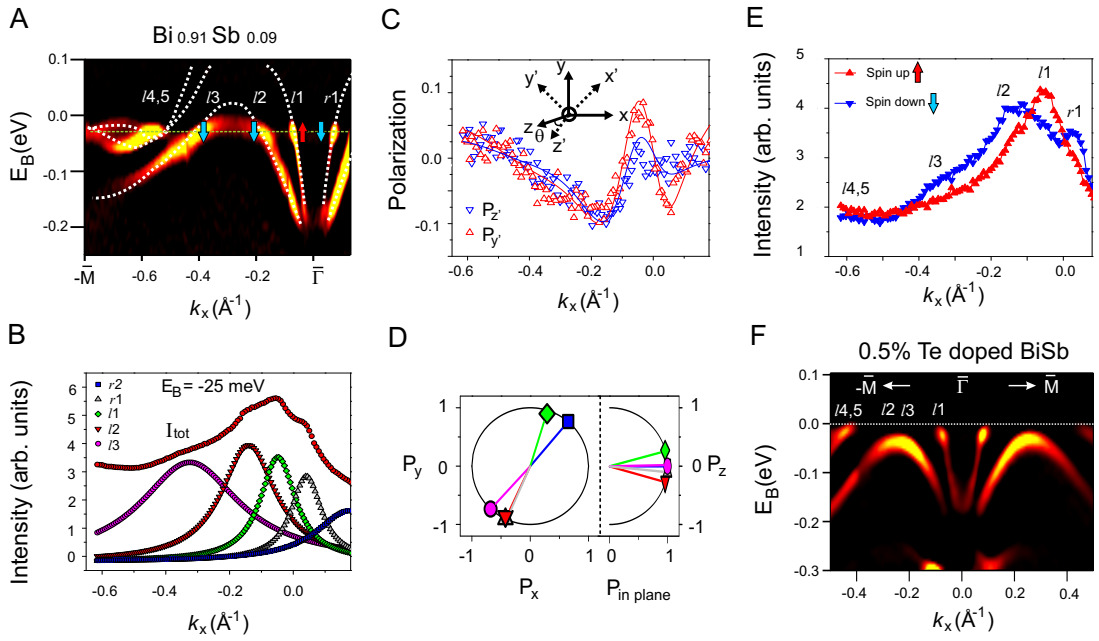


FIG. S1: (**A**) The surface band dispersion ARPES second derivative image (SDI) along the $\bar{\Gamma}$ to -$\bar{\text{M}}$ direction of bulk insulating $Bi_{0.91}Sb_{0.09}$. Dashed white lines are guides to the eye. The intensity of bands $l4,5$ is scaled up for clarity. (**B**) MDC of the spin averaged spectrum at $E_B$ = -25 meV [green line below $E_F$ in (**A**)] using a photon energy $h\nu = 22$ eV, together with the Lorentzian peaks of the fit. (**C**) Measured spin polarization curves (symbols) for the $y'$ and $z'$ (Mott coordinate) components together with the fitted lines (see SOM B text). The relative orientation of the sample (un-primed) to Mott (primed) coordinates is shown in the inset. The polar angle $\theta$ is rotated during the measurement to access different values of $k_x$. At normal emission ($\theta = 0°$), the $z'$ and $z$ axes are parallel and the $y'$ axis is rotated from the $y$ axis by 45°. (**D**) The in-plane and out-of-plane spin polarization components in the sample coordinate frame obtained from the spin polarization fit. The symbols refer to those in (**B**). The fitted parameters are consistent with 100% polarized spins. (**E**) Spin resolved spectra for the $y$ component based on the fitted spin polarization curves shown in (**C**). Spin up (down) refers to the spin direction being approximately parallel to the +(-)$\hat{y}$ direction. (**F**) The surface band dispersion SDI centered about $\bar{\Gamma}$ of $(Bi_{0.925}Sb_{0.075})_{0.995}Te_{0.005}$. Electron doping through Te reveals that bands $l2$ and $l3$ are connected above $E_F$.

-$\bar{\text{M}}$ direction taken at $E_B$ = -25 meV, indicated by the green line shown in Figure S1(A). This MDC was obtained by summing the signal coming from both left and right electron detectors in the Mott polarimeter (see diagram in Fig.3(A) of the main text). Lorentzian lineshapes

denoted $I^i$ and a non-polarized background $B$ are fitted to this MDC, which are used as inputs to the two-step fitting routine developed by Meier *et al.* (26) in the following way. To begin with, a spin polarization vector $\vec{P}^i_M = (P^i_{x'}, P^i_{y'}, P^i_{z'}) = (\cos\theta_i \cos\phi_i, \cos\theta_i \sin\phi_i, \sin\theta_i)$ is assigned to each band, where $\theta_i$ and $\phi_i$ are referenced to the primed Mott coordinate frame. Here it is necessary to assume a spin magnitude of one because only two spin components are measured by a single Mott detector. Such an assumption is likely valid since even though the spin polarization is no longer a good quantum number due to spin-orbit coupling, the bands near $\bar{\Gamma}$ are expected to exhibit a high degree of spin polarization since the spin-orbit coupling is smallest near $\bar{\Gamma}$. Moreover, common strong spin-orbit coupled materials such as gold have been experimentally shown to exhibit 100% spin polarized surface states (18). A spin-resolved spectrum is then defined for each peak $i$ using $I^{i;\uparrow,\downarrow}_\alpha = I^i(1 \pm P^i_\alpha)/6$, where $\alpha = x', y', z'$, and $+$ and $-$ correspond to the spin direction being parallel ($\uparrow$) or antiparallel ($\downarrow$) to $\alpha$. The full spin-resolved spectrum is then given by $I^{\uparrow,\downarrow}_\alpha = \sum_i I^{i;\uparrow,\downarrow}_\alpha + B/6$, where $B$ is the unpolarized background, from which the spin polarization of each spatial component can be obtained as $P_\alpha = (I^\uparrow_\alpha - I^\downarrow_\alpha)/(I^\uparrow_\alpha + I^\downarrow_\alpha)$. This latter expression is a function of $\theta_i$ and $\phi_i$ and is used to fit to the experimental data.

The spin polarization data for the $y'$ and $z'$ components (i.e. $P_{y'}$ and $P_{z'}$) are obtained by taking the difference between the intensities of the left-right (or top-bottom) electron detectors over their sum, all divided by the Sherman function, which is calibrated using the methods in (S1, p.36). Typical electron counts on the detector reach $5 \times 10^5$, which places an error bar of approximately $\pm 0.01$ for each point on our polarization curves. To account for unequal sensitivities between a detector pair, we applied a small multiplicative factor to the intensity from one detector to ensure that the unpolarized background intensity yields zero polarization. Resultant curves are shown in Figure S1(C). The best fit parameters $(P^i_{x'}, P^i_{y'}, P^i_{z'})$, which are expressed in the sample coordinates through an appropriate coordinate transformation [inset of Fig. S1(C)] are shown in Figure S1(D). Even though the measured polarization only reaches a magnitude of around $\pm 0.1$, this is similarly seen in studies of Bi thin films (S4) and is due to the non-polarized background and overlap of adjacent peaks with different spin polarization. These effects are extremely sensitive to the sample alignment due to the very narrow Fermi surface features. The fitted parameters [Fig. S1(D)] are consistent with spins being nearly aligned along the $\pm\hat{y}$ direction, with bands $l1$ and $r1$ having nearly opposite spin as required by time reversal symmetry, and

with these spins nearly parallel to those of $l1$ and $r1$ respectively measured for Sb [main text Fig.3(F)]. The small departures from ideality likely originate from the scan direction not being exactly along $\bar{\Gamma}$-$\bar{\mathrm{M}}$. Bands $l1$ and $l2$ display opposite spin, which indicates that they form a Kramers pair split by spin-orbit coupling, and the fact that bands $l2$ and $l3$ have the same spin suggests that they originate from the same band.

To show that bands $l2$ and $l3$ connect above $E_F$ as we have drawn in Figure S1(A), and are thus expected to have the same spin, we map the surface band dispersion of Te doped $Bi_{1-x}Sb_x$ that is known to be an electron donor (S5). Figure S1(F) shows that the hole band formed by crossings 2 and 3 in insulating $Bi_{1-x}Sb_x$ [Fig. S1(A)] has sunk completely below $E_F$ with 0.5% Te doping, and is in fact the same band.

## SOM C. Method of using incident photon energy modulated ARPES to separate the bulk from surface electronic states of Sb

In this section we detail incident photon energy modulated ARPES experiments on the low lying electronic states of single crystal Sb(111), which we employ to isolate the surface from bulk-like electronic bands over the entire BZ. Figure S2(C) shows momentum distributions curves (MDCs) of electrons emitted at $E_F$ as a function of $k_x$ ($\parallel \bar{\Gamma}$-$\bar{\mathrm{M}}$) for Sb(111). The out-of-plane component of the momentum $k_z$ was calculated for different incident photon energies ($h\nu$) using the free electron final state approximation with an experimentally determined inner potential of 14.5 eV (S7, S8). There are four peaks in the MDCs centered about $\bar{\Gamma}$ that show no dispersion along $k_z$ and have narrow widths of $\Delta k_x \approx 0.03$ Å$^{-1}$. These are attributed to surface states and are similar to those that appear in Sb(111) thin films (S7). As $h\nu$ is increased beyond 20 eV, a broad peak appears at $k_x \approx$ -0.2 Å$^{-1}$, outside the $k$ range of the surface states near $\bar{\Gamma}$, and eventually splits into two peaks. Such a strong $k_z$ dispersion, together with a broadened linewidth ($\Delta k_x \approx 0.12$ Å$^{-1}$), is indicative of bulk band behavior, and indeed these MDC peaks trace out a Fermi surface [Fig. S2(D)] that is similar in shape to the hole pocket calculated for bulk Sb near H (S6). Therefore by choosing an appropriate photon energy (e.g. $\leq$ 20 eV), the ARPES spectrum at $E_F$ along $\bar{\Gamma}$-$\bar{\mathrm{M}}$ will have contributions from only the surface states. The small bulk electron pocket centered at L is not accessed using the photon energy range we employed [Fig. S2(D)].

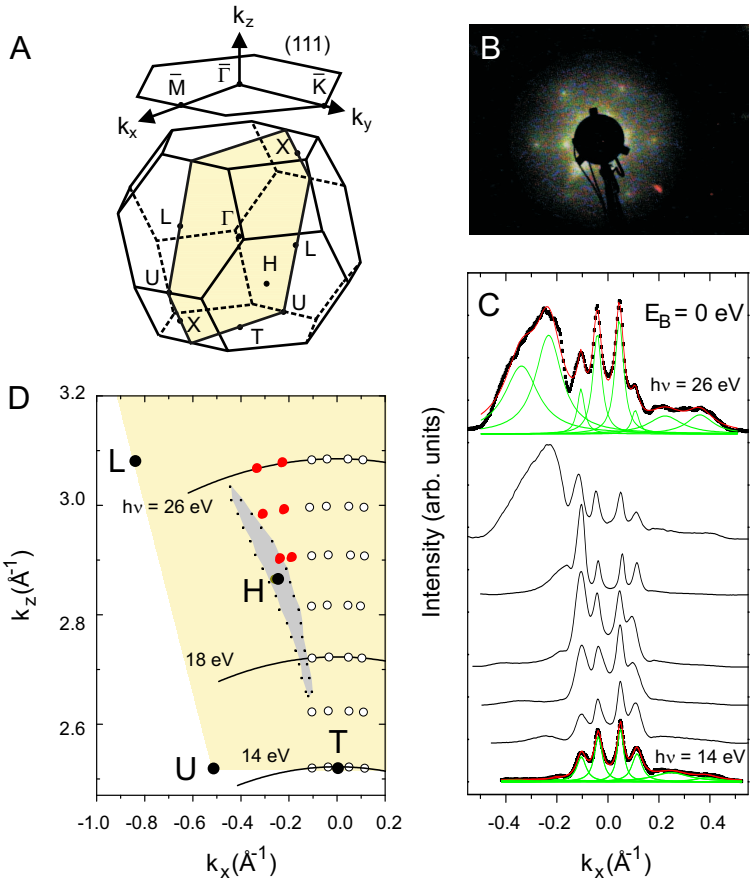


FIG. S2: (**A**) Schematic of the bulk BZ of Sb and its (111) surface BZ. The shaded region denotes the momentum plane in which the following ARPES spectra were measured. (**B**) LEED image of the *in situ* cleaved (111) surface exhibiting a hexagonal symmetry. (**C**) Select MDCs at $E_F$ taken with photon energies from 14 eV to 26 eV in steps of 2 eV, taken in the $TXLU$ momentum plane. Peak positions in the MDCs were determined by fitting to Lorentzians (green curves). (**D**) Experimental 3D bulk Fermi surface near H (red circles) and 2D surface Fermi surface near $\bar{\Gamma}$ (open circles) projected onto the $k_x$-$k_z$ plane, constructed from the peak positions found in (**C**). The $k_z$ values are determined using calculated constant $h\nu$ contours (black curves) (see SOM C text). The shaded gray region is the theoretical hole Fermi surface calculated in (S6).

Now we describe the experimental procedure used to distinguish pure surface states from resonant states on Sb(111) through their spectral signatures. ARPES spectra along $\bar{\Gamma}$-$\bar{\mathrm{M}}$ taken at three different photon energies are shown in Fig. S3. Near $\bar{\Gamma}$ there are two rather linearly dispersive electron like bands that meet exactly at $\bar{\Gamma}$ at a binding energy $E_B \sim$

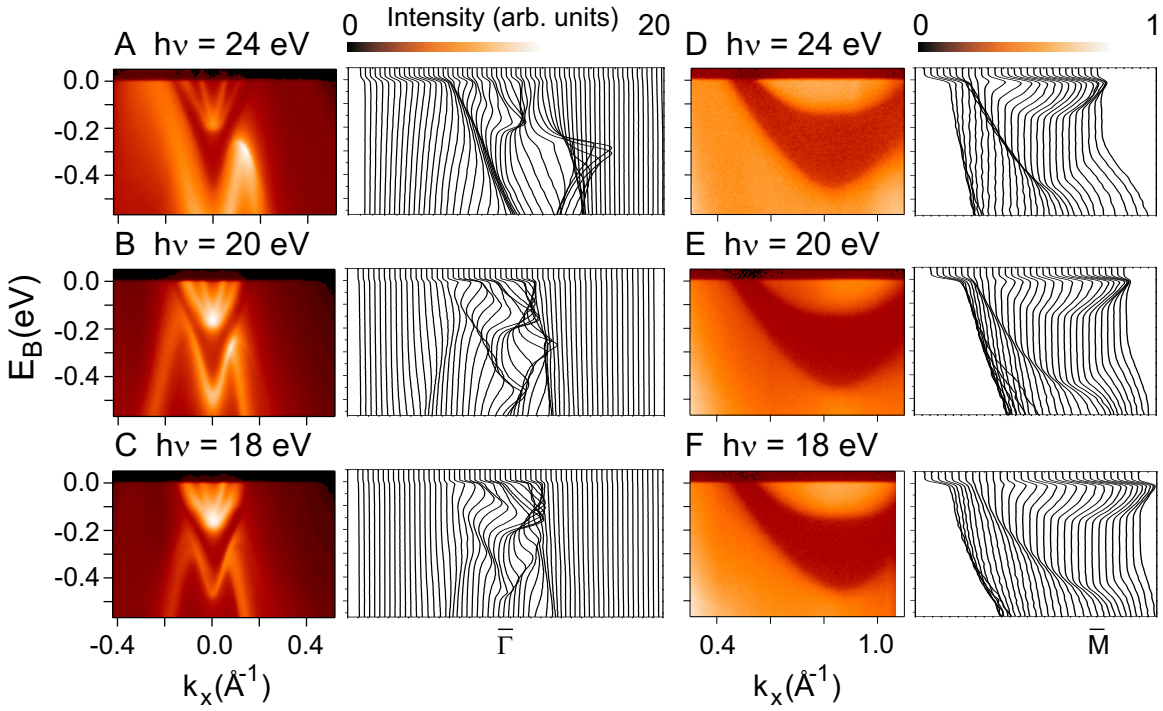


FIG. S3: ARPES intensity maps of Sb(111) as a function of $k_x$ near $\bar{\Gamma}$ (**A**)-(**C**) and $\bar{\mathrm{M}}$ (**D**)-(**F**) and their corresponding energy distribution curves, taken using $h\nu = 24$ eV, 20 eV and 18 eV photons. The intensity scale of (**D**)-(**F**) is a factor of about twenty smaller than that of (**A**)-(**C**) due to the intrinsic weakness of the ARPES signal near $\bar{\mathrm{M}}$.

-0.2 eV. This behavior is consistent with a pair of spin-split surface bands that become degenerate at the time reversal invariant momentum ($\vec{k}_T$) $\bar{\Gamma}$ due to Kramers degeneracy. The surface origin of this pair of bands is established by their lack of dependence on $h\nu$ [Fig. S3(A)-(C)]. A strongly photon energy dispersive hole like band is clearly seen on the negative $k_x$ side of the surface Kramers pair, which crosses $E_F$ for $h\nu = 24$ eV and gives rise to the bulk hole Fermi surface near H [Fig. S2(D)]. For $h\nu \leq 20$ eV, this band shows clear back folding near $E_B \approx$ -0.2 eV indicating that it has completely sunk below $E_F$. Further evidence for its bulk origin comes from its close match to band calculations [Fig. S2(D)]. Interestingly, at photon energies such as 18 eV where the bulk bands are far below $E_F$, there remains a uniform envelope of weak spectral intensity near $E_F$ in the shape of the bulk hole pocket seen with $h\nu = 24$ eV photons, which is symmetric about $\bar{\Gamma}$. This envelope does not change shape with $h\nu$ suggesting that it is of surface origin. Due to its weak intensity relative to states at higher binding energy, these features cannot be easily seen

in the energy distribution curves (EDCs) in Fig. S3(A)-(C), but can be clearly observed in the MDCs shown in Fig. S2(C) especially on the positive $k_x$ side. Centered about the $\bar{\mathrm{M}}$ point, we also observe a crescent shaped envelope of weak intensity that does not disperse with $k_z$ [Fig. S3(D)-(F)], pointing to its surface origin. Unlike the sharp surface states near $\bar{\Gamma}$, the peaks in the EDCs of the feature near $\bar{\mathrm{M}}$ are much broader ($\Delta E$ ∼80 meV) than the spectrometer resolution (15 meV). The origin of this diffuse ARPES signal is not due to surface structural disorder because if that were the case, electrons at $\bar{\Gamma}$ should be even more severely scattered from defects than those at $\bar{\mathrm{M}}$. In fact, the occurrence of both sharp and diffuse surface states originates from a $k$ dependent coupling to the bulk. As seen in Fig.2(D) of the main text, the spin-split Kramers pair near $\bar{\Gamma}$ lie completely within the gap of the projected bulk bands near $E_F$ attesting to their purely surface character. In contrast, the weak diffuse hole like band centered near $k_x = 0.3$ Å$^{-1}$ and electron like band centered near $k_x = 0.8$ Å$^{-1}$ lie completely within the projected bulk valence and conduction bands respectively, and thus their ARPES spectra exhibit the expected lifetime broadening due to coupling with the underlying bulk continuum (S9).

## SOM D. Method of counting spin Fermi surface $\vec{k}_T$ enclosures in pure Sb

In this section we give a detailed explanation of why the surface Fermi contours of Sb(111) that overlap with the projected bulk Fermi surfaces can be neglected when determining the $\nu_0$ class of the material. Although the Fermi surface formed by the surface resonance near $\bar{\mathrm{M}}$ encloses the $\vec{k}_T$ $\bar{\mathrm{M}}$, we will show that this Fermi surface will only contribute an even number of enclosures and thus not alter the overall evenness or oddness of $\vec{k}_T$ enclosures. Consider some time reversal symmetric perturbation that lifts the bulk conduction $\mathrm{L}_a$ band completely above $E_F$ so that there is a direct excitation gap at L. Since this perturbation preserves the energy ordering of the $\mathrm{L}_a$ and $\mathrm{L}_s$ states, it does not change the $\nu_0$ class. At the same time, the weakly surface bound electrons at $\bar{\mathrm{M}}$ can evolve in one of two ways. In one case, this surface band can also be pushed up in energy by the perturbation such that it remains completely inside the projected bulk conduction band [Fig. S4(A)]. In this case there is no more density of states at $E_F$ around $\bar{\mathrm{M}}$. Alternatively the surface band can remain below $E_F$ so as to form a pure surface state residing in the projected bulk gap. However by

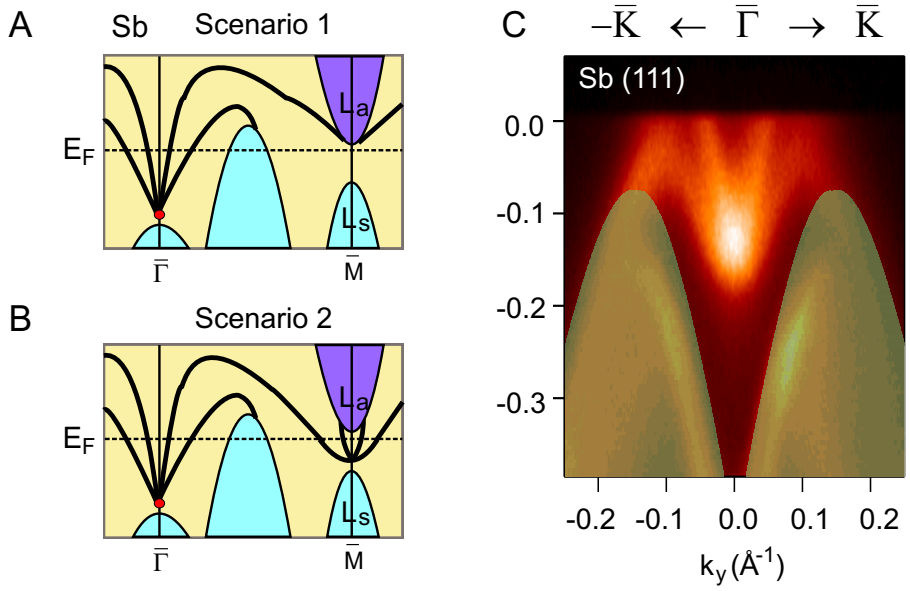


FIG. S4: (**A**) Schematic of the surface band structure of Sb(111) under a time reversal symmetric perturbation that lifts the bulk conduction ($L_a$) band above the Fermi level ($E_F$). Here the surface bands near $\bar{M}$ are also lifted completed above $E_F$. (**B**) Alternatively the surface band near $\bar{M}$ can remain below $E_F$ in which case it must be doubly spin degenerate at $\bar{M}$. (**C**) ARPES intensity plot of the surface states along the -$\bar{K}$−$\bar{\Gamma}$−$\bar{K}$ direction. The shaded green regions denote the theoretical projection of the bulk valence bands, calculated using the full potential linearized augmented plane wave method using the local density approximation including the spin-orbit interaction (method described in S10). Along this direction, it is clear that the outer V-shaped surface band that was observed along the -$\bar{M}$−$\bar{\Gamma}$−$\bar{M}$ now merges with the bulk valence band.

Kramers theorem, this SS must be doubly spin degenerate at $\bar{M}$ and its FS must therefore enclose $\bar{M}$ twice [Fig. S4(B)]. In determining $\nu_0$ for semi-metallic Sb(111), one can therefore neglect all segments of the FS that lie within the projected areas of the bulk FS [Fig.2(G) of main text] because they can only contribute an even number of FS enclosures, which does not change the modulo 2 sum of $\vec{k}_T$ enclosures.

In order to further experimentally confirm the topologically non-trivial surface band dispersion shown in figures 2(C) and (D) of the main text, we show ARPES intensity maps of Sb(111) along the -$\bar{K}$−$\bar{\Gamma}$−$\bar{K}$ direction. Figure S4(C) shows that the inner V-shaped band that was observed along the -$\bar{M}$−$\bar{\Gamma}$−$\bar{M}$ direction retains its V-shape along the -$\bar{K}$−$\bar{\Gamma}$−$\bar{K}$ direction and continues to cross the Fermi level, which is expected since it forms the

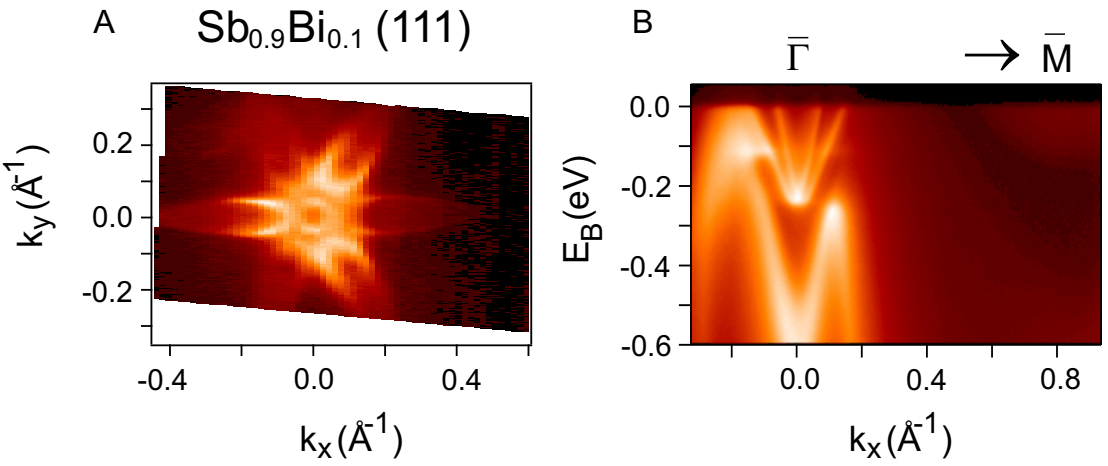


FIG. S5: Spin split surface states survive alloying disorder in $Sb_{0.9}Bi_{0.1}$. (**A**) ARPES intensity map at $E_F$ of single crystal $Sb_{0.9}Bi_{0.1}(111)$ in the $k_x$-$k_y$ plane taken using 20 eV photons. (**B**) ARPES intensity map of $Sb_{0.9}Bi_{0.1}(111)$ along the $\bar{\Gamma}$-$\bar{M}$ direction taken with $h\nu = 22$ eV photons. The band dispersion is not symmetric about $\bar{\Gamma}$ because of the three-fold rotational symmetry of the bulk states about the $\langle 111 \rangle$ axis.

central hexagonal Fermi surface. On the other hand, the outer V-shaped band that was observed along the -$\bar{M}$−$\bar{\Gamma}$−$\bar{M}$ direction no longer crosses the Fermi level along the -$\bar{K}$−$\bar{\Gamma}$−$\bar{K}$ direction, instead folding back below the Fermi level around $k_y = 0.1$ Å$^{-1}$ and merging with the bulk valence band [Fig. S4(C)]. This confirms that it is the $\Sigma_{1(2)}$ band starting from $\bar{\Gamma}$ that connects to the bulk valence (conduction) band, in agreement with the calculations shown in figure 2(D) of the main text.

## SOM E. Investigation of the robustness of Sb spin states under random field perturbations introduced by Bi substitutional disorder

The predicted topological protection of the surface states of Sb implies that their metallicity cannot be destroyed by weak time reversal symmetric perturbations. In order to test the robustness of the measured gapless surface states of Sb, we introduce such a perturbation by randomly substituting Bi into the Sb crystal matrix (SOM A). Another motivation for performing such an experiment is that the formalism developed by Fu and

Kane (S11) to calculate the $Z_2$ topological invariants relies on inversion symmetry being present in the bulk crystal, which they assumed to hold true even in the random alloy $Bi_{1-x}Sb_x$. However, this formalism is simply a device for simplifying the calculation and the non-trivial $\nu_0 = 1$ topological class of $Bi_{1-x}Sb_x$ is predicted to hold true even in the absence of inversion symmetry in the bulk crystal (S11). Therefore introducing light Bi substitutional disorder into the Sb matrix is also a method to examine the effects of alloying disorder and possible breakdown of bulk inversion symmetry on the surface states of Sb(111). We have performed spin-integrated ARPES measurements on single crystals of the random alloy $Sb_{0.9}Bi_{0.1}$. Figure S5 shows that both the surface band dispersion along $\bar{\Gamma}$-$\bar{M}$ as well as the surface state Fermi surface retain the same form as that observed in Sb(111), and therefore the 'topological metal' surface state of Sb(111) fully survives the alloy disorder. Since Bi alloying is seen to only affect the band structure of Sb weakly, it is reasonable to assume that the topological order is preserved between Sb and $Bi_{0.91}Sb_{0.09}$ as we observed.

## SOM F. Physical interpretation of $n_M$ : the mirror Chern number and an analogy with the spin-Chern number

In this section we will describe how a mirror Chern number arises from the crystal symmetry of $Bi_{1-x}Sb_x$. Electronic states in the mirror plane ($k_y = 0$) [Fig. S6(A)] are eigenstates of the mirror operator $M(\hat{y})$ with eigenvalues $\pm i$. $M(\hat{y})$ is closely related to, but not exactly the same as the spin operator $S_y$. It may be written as $M(\hat{y}) = PC_2(\hat{y})$: the product of the parity operator $P : (x, y, z) \rightarrow (-x, -y, -z)$ and a twofold rotation operator $C_2(\hat{y})$: $(x, y, z) \rightarrow (-x, y, -z)$. For a free spin, $P$ does not affect the pseudovector spin, and $C_2(\hat{y})$ simply rotates the spin. Thus, $M(\hat{y}) = \exp[-i\pi S_y/\hbar]$. For spin eigenstates $S_y = \pm\hbar/2$, this gives $M(\hat{y}) = \mp i$. In the crystal with spin-orbit interaction on the other hand, $S_y$ is no longer a good quantum number, but $M(\hat{y})$ still is. The energy bands near the Fermi energy in $Bi_{1-x}Sb_x$ are derived from states with even orbital mirror symmetry and satisfy $M(\hat{y}) \propto -i\ \mathrm{sign}(\langle S_y \rangle)$, as detailed in S12 and summarized below.

Unlike the bulk states which are doubly spin degenerate, the surface state spin degeneracy is lifted due to the loss of crystal inversion symmetry at the surface, giving rise to the typical Dirac like dispersion relations near time reversal invariant momenta [Fig. S6(B)&(C)]. For surface states in the mirror plane $k_y = 0$ with $M(\hat{y}) = \pm i$, the spin split dispersion near

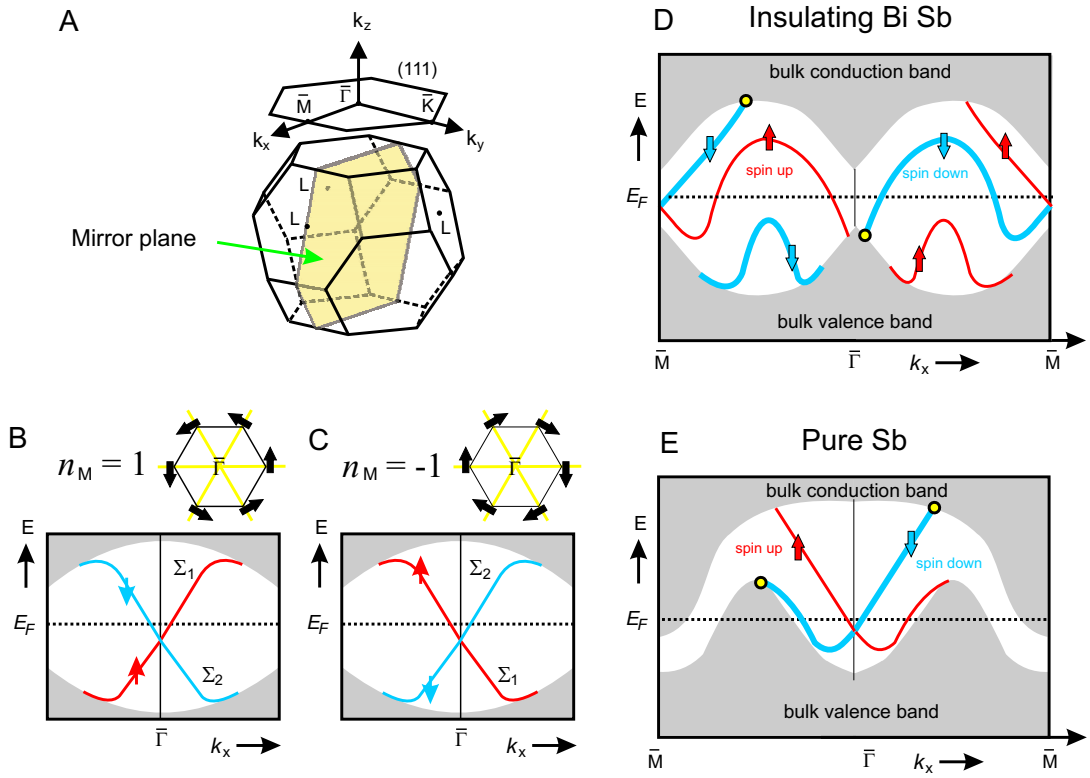


FIG. S6: Implications of k-space mirror symmetry on the surface spin states. (**A**) 3D bulk Brillouin zone and the mirror plane in reciprocal space. (**B**) Schematic spin polarized surface state band structure for a mirror Chern number ($n_M$) of +1 and (**C**) -1. Spin up and down mean parallel and anti-parallel to $\hat{y}$ respectively. The upper (lower) shaded gray region corresponds to the projected bulk conduction (valence) band. The hexagons are schematic spin polarized surface Fermi surfaces for different $n_M$, with yellow lines denoting the mirror planes. (**D**) Schematic representation of surface state band structure of insulating $Bi_{1-x}Sb_x$ and (**E**) semi metallic Sb both showing a $n_M = -1$ topology. Yellow circles indicate where the spin down band (bold) connects the bulk valence and conduction bands.

$k_x = 0$ has the form $E = \pm\hbar v k_x$. Assuming no other band crossings occur, the sign of the velocity $v$ is determined by the topological mirror Chern number ($n_M$) describing the bulk band structure. When $n_M = 1$, the situation in figure S6(B) is realized where it is the spin up ($\langle S_y \rangle \parallel \hat{y}$) band that connects the bulk valence to conduction band going in the positive $k_x$ direction (i.e. the spin up band has a velocity in the positive $x$ direction). For $n_M = -1$ the opposite holds true [Fig. S6(C)]. These two possibilities also lead to two distinct chiralities of the central Fermi surface as shown in figures S6(B)&(C). From our spin-

resolved ARPES data on both insulating $Bi_{1-x}Sb_x$ and pure Sb, we find that the surface polarized band dispersions are consistent with $n_M = -1$ [Figs S6(D)&(E)], suggesting that their bulk electron wavefunctions exhibit the anomalous value $n_M = -1$ predicted in (S12), which is not realizable in free electron systems with full rotational symmetry.

There is an intimate physical connection between a 2D quantum spin Hall insulator and the 2D k-space mirror plane of a 3D topological insulator. In the former case, the occupied energy bands for each spin eigenvalue will be associated with an ordinary Chern integer $n_{\uparrow,\downarrow}$, from which a non-zero spin-Chern number can be defined $n_s = (n_\uparrow - n_\downarrow)/2$. In the latter case, it is the mirror eigenvalue of the occupied energy bands that have associated with them Chern integers $n_{+i,-i}$, from which a non-zero mirror Chern number can be defined $n_M = (n_{+i} - n_{-i})/2$.

## References


**S1.** M. Hoesch, PhD dissertation, University of Zürich, (2002)

**S2.** S. Bengió *et al.*, *Surface Science* **601**, 2908 (2007).

**S3.** P. D. Johnson. *Rep. Prog. Phys.* **60**, 1217 (1997).

**S4.** T. Hirahara *et al.*, *Phys. Rev.* **B76**, 153305 (2007).

**S5.** D. M. Brown, S. J. Silverman, *Phys. Rev.* **136**, A290 (1964).

**S6.** L. M. Falicov, P. J. Lin, *Phys. Rev.* **141**, 562 (1965).

**S7.** H. Höchst, C. R. Ast, *J. Electron Spectrosc. Relat. Phenom.* **137**, 441 (2004).

**S8.** X. Gonze *et al.*, *Phys. Rev.* **B44**, 11023 (1991).

**S9.** E. Kneedler, K. E. Smith, D. Skelton, S. D. Kevan, *Phys. Rev.* **B44**, 8233 (1991).

**S10.** Yu. M. Koroteev *et al.*, *Phys. Rev. Lett.* **93**, 046403 (2004).

**S11.** L. Fu, C. L. Kane, *Phys. Rev.* **B76**, 045302 (2007).

**S12.** J. C. Y. Teo, L. Fu, C. L. Kane, *Phys. Rev.* **B78**, 045426 (2008).



Correspondence and requests for materials should be addressed to M.Z.H. (Email: mzhasan@princeton.edu).